coatings

MDPI

Article

Statistical/Numerical Model of the Powder-Gas Jet for Extreme High-Speed Laser Material Deposition

Thomas Schopphoven [1,*], Norbert Pirch [1], Stefan Mann [1], Reinhart Poprawe [1], Constantin Leon Häfner [1,2] and Johannes Henrich Schleifenbaum [1,3]

[1] Fraunhofer Institute for Laser Technology ILT, 52074 Aachen, Germany; norbert.pirch@ilt.fraunhofer.de (N.P.); stefan.mann@ilt.fraunhofer.de (S.M.); reinhart.poprawe@ilt.fraunhofer.de (R.P.); constantin.haefner@ilt.fraunhofer.de (C.L.H.); johannes.henrich.schleifenbaum@ilt.fraunhofer.de (J.H.S.)
[2] Chair for Laser Technology LLT, RWTH Aachen University, 52074 Aachen, Germany
[3] Chair for Digital Additive Production DAP, RWTH Aachen University, 52074 Aachen, Germany
* Correspondence: thomas.schopphoven@ilt.fraunhofer.de; Tel.: +49-(0)241-8906-8107

Received: 18 March 2020; Accepted: 13 April 2020; Published: 22 April 2020

Abstract: Extreme high-speed laser material deposition, known by its German acronym EHLA, is a new variant of laser material deposition (LMD) with powdered additives. This variant's process control is unlike that of LMD, where the powder melts as it contacts the melt pool. In the EHLA process, the laser beam melts the powder above the surface of the substrate to deliver a liquid to the melt pool. At a given intensity distribution in a laser beam, the heating of powder particles in the beam path depends largely on the three-dimensional powder particle density distribution (PDD) and the relative position within the laser beam caustic. As a key element of a comprehensive numerical process model for EHLA, this paper presents a statistical/numerical model of the powder-gas jet, as previously published in Experimentelle und modelltheoretische Untersuchungen zum Extremen Hochgeschwindigkeits-Laserauftragschweißen. The powder-gas jet is characterized experimentally and described with a mathematical model. This serves to map the PDD of the powder-gas flow—and particularly the particle trajectories for different grain fractions—as well as the powder mass flows and carrier and inert gas settings, to a theoretical model. The result is a numerical description of the particle trajectories that takes into account the measured particle size distribution with calculations made on the assumption of a constant particle velocity and linear trajectories of the particles.

Keywords: extreme high-speed laser material deposition (EHLA); laser material deposition (LMD); coaxial powder nozzle; coating; additive manufacturing; numerical simulation

1. Introduction

Laser material deposition (LMD) is a process by which a laser beam creates a melt pool on the surface of a substrate while a powder nozzle delivers a powdered additive to the processing point–that is, into the melt pool. To produce a metallurgically bonded layer that is free of defects, the laser power, feed rate, powder mass flow and other process parameters have to be configured so as to apply sufficient process heat to trigger a suitable temperature–time cycle for the base material and additive. This application of heat goes to create a melt pool on the substrate surface and ensures that the additive melts fully. The relative motion of the laser beam and/or substrate leaves a dense, metallurgically bonded weld bead after the melt pool solidifies. A coating may be applied over a wider area by overlapping several weld beads. Multiple layers may be deposition-welded on top of one another, so the process may also be used for repair, additive manufacturing and hybrid additive manufacturing–that is, additive manufacturing on top of cast, forged or otherwise conventionally

made base geometries, for example, to modify a part's geometry. Figure 1 diagrams the key factors influencing the process of forming a metallurgically bonded composite [1].

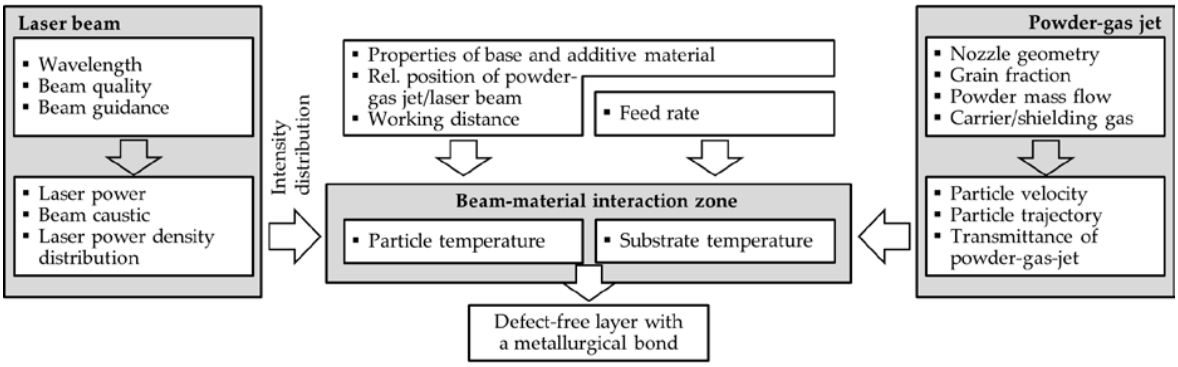

Figure 1. Diagram of the factors influencing powder-based laser material deposition (LMD) [1]. Reprinted with permission from Ref [1]. Copyright 2020, Fraunhofer Verlag.

In a heat balance equation for the melt pool's surface, the heat flow is the product of the thermalized, transmitted radiation less the heat flow induced by the temperature equalization between the powder particles and the melt pool's surface as well as the heat loss attributable to radiation. Equation (1) is a mathematical description of the heat balance at the melt pool's surface with the proportion of transmitted radiation I_{trans}, of the powder mass flow $\dot{m}_p$, the temperature-dependent specific heat capacity c_p of the material density ρ_p, the emissivity ε, the Stefan-Boltzmann constant σ, the temperature equalization between the temperature at the melt pool's surface T_S and the mean particle temperature T_p [2,3]:

$$\lambda\langle\nabla T, \vec{n}\rangle = \langle \vec{I}_{trans}[x(t), y(t)], \vec{n}\rangle - \dot{m}_p\rho_p c_p(T_S - T_P) - \varepsilon\sigma T^4 \quad (1)$$

Depending on the difference between the particle and melt pool temperatures $(T_s - T_p)$, the second term is a source or loss term for which a corresponding heat of fusion must be considered in the event that particle temperatures are lower than the melting temperature T_M, [2]. A distinction between two different process control strategies is to be made depending on the temperature of particles before they enter the melt pool: For one, there is conventional LMD with particle temperatures that are predominantly lower than the melting temperature $T_p < T_M$, or $(T_s - T_p) > 0$. For the other, there is the extreme high-speed laser material (EHLA) process in which a large share of the particles are to be fully melted by the laser beam before they arrive in the melt pool $T_p > T_M$, or $(T_s - T_p) < 0$ [1,4–7].

1.1. Process Ccontrol in Laser Material Deposition

Figure 2 illustrates the principle of the conventional LMD process with a continuous coaxial powder nozzle. The interaction time between powder particles and the laser beam is relatively short. The temperature of particles before they enter the melt pool is usually far lower than the melting temperature, so the particles are not melted fully until they arrive in the melt pool [8–11]. In the process control used to date, most of the laser beam's radiation is transmitted to the substrate, depending on the type of powder nozzles used, the grain fraction, the relative positions of the powder nozzle and the laser beam, and the working distance. This results in a relatively large heat-affected zone with dimensions ranging from a few tenths of a millimeter to one millimeter [1,11–17].

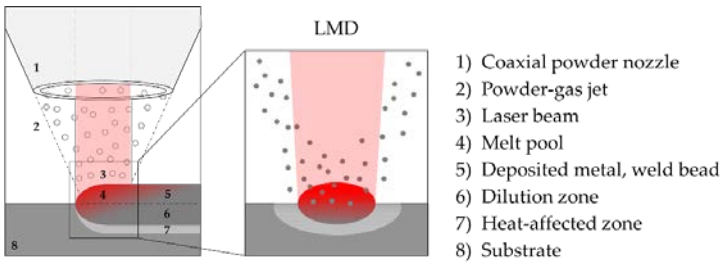

Figure 2. A diagram of the principle behind the LMD process [1]. Reprinted with permission from Ref [1]. Copyright 2020, Fraunhofer Verlag.

1.2. Process Control in Extreme High-Speed Laser Material Deposition

Unlike the process control for LMD, where the powder melts as it contacts the melt pool, in the EHLA process, the laser beam melts the powder above the surface of the substrate to deliver a liquid to the melt pool. Saving time otherwise required to melt the particles in the melt pool, this can increase the achievable feed rate from a few meters per minute to up to several hundred meters per minute [4–7]. Figure 3 illustrates the principle of the EHLA process. To this end, the ratio of transmitted laser radiation to the laser radiation absorbed by the powder particles has to be adjusted so that the heat input is sufficient to fully melt the particles already in the beam path and to create a melt pool on the surface of the substrate [7].

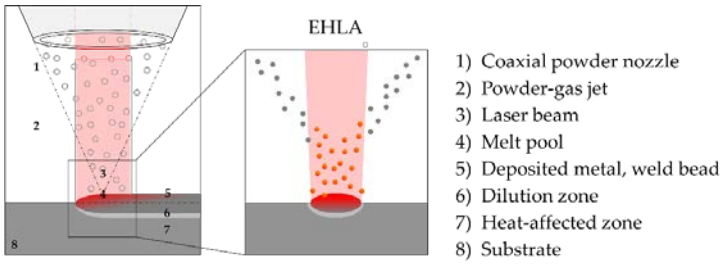

Figure 3. Diagram of the principle behind the extreme high-speed laser material deposition (EHLA) process [1]. Reprinted with permission from Ref [1]. Copyright 2020, Fraunhofer Verlag.

The key influencing factors on the heating of powder particles in the beam path above the melt pool are the powder particle trajectories, the particle velocity, the particle fraction and the relative position to the laser beam caustic. The additive's specific heat capacity, density, absorption coefficient and other thermophysical and optical properties also have an influence. The particles' trajectories and velocities determine the three-dimensional particle density distribution (PDD). However, as it stands given the current state of the art, there are no EHLA process control tools or methods available to describe the PDD for determining process-relevant influencing factors such as transmittance, particle heating in the beam path, substrate heating and track formation [1].

1.3. Modelling of the Powder-Gas Jet or Powder Particle Density Distribution

The formation of the powder-gas jet (particle velocity and trajectory) and thus the powder particle density distribution depends not only on the given nozzle's design and geometry. The powder grain fraction and the powder feed process parameters (powder mass flow, carrier and shielding gas volume flow) are also key determinants. The powder–gas flow is a dispersed, diluted two-phase solid flow consisting of the powder particles (disperse phase) and the carrier gas (continuous phase). Particle-to-particle and particle-to-nozzle wall collisions may occur depending on the degree of reciprocal action [18–22]. The particles are introduced into the upper part of the powder nozzle with the carrier gas so that their distribution is homogenized across the cross section by means of particle-to-wall collisions up to the nozzle outlet. The powder-gas flow exits the tip of the nozzle to

enter an ambient medium with the shielding gas. Then turbulent mixing and swirling with the ambient medium causes the formation of a free jet [23–27]. Aligning the powder-gas jet on the substrate's surface transforms this original free jet into an impact jet. Contact with the substrate's surface reduces the gas flow velocity in the direction of the beam axis to zero [28–30]. The particles' velocities are reduced as a function of the particle following behavior, whereby the powder particles may still retain enough velocity to be fully immersed into the melt. The powder-gas flow is fully described by the volume-related conservation laws of mass, momentum and energy (the Navier-Stokes equations). However, the flow processes are so complex that at present they cannot be simulated without assuming simplified boundary conditions. Only the particles' trajectories and velocities prior to the nozzle's outlet are relevant to the interaction with the laser beam, which–depending on the given grain fraction and powder mass flow–determine the transmittance of the powder-gas jet and heating of the particles before they contact the substrate. Numerical and analytical models with varying depths of detail, scopes and assumptions for the mathematical definition of the powder-gas jet forming behind the nozzle tip are described in the literature. In most cases, the powder-gas jet is described numerically with the standard k-ε turbulence model for turbulent two-phase flows [31–35]. The k-ε model is a transport equation for a viscous vortex model in which the turbulent flow is described with the two parameters k for the turbulent kinetic energy and ε for the dissipation rate. The details of the two-phase flow within the nozzle are irrelevant to understanding the process and describing the particles' interaction with the laser beam–unless the goal is to learn what measures need to be taken to adapt the nozzle's design for a given purpose, for example, to achieve certain particle velocities or trajectories. Analytical descriptions of the powder-gas jet usually approximate the powder particle density distribution on the basis of a two-dimensional, radially symmetrical Gaussian distribution. To this end, the free parameters of the normal distribution pattern are defined according to the nozzle's geometry and a comparison to experimental results. Because the Gaussian distribution is radially symmetrical, these models are only valid forward of the point at which the powder-gas jet's hollow cone consolidates (the powder focus). The area prior to the point at which the annular powder distribution consolidates is not modeled at all [36–39] or approximated by partial jets [40–42]–either that, or it is assumed that the particle density distribution (PDD) of the powder-gas jet takes on a Gaussian shape immediately after the nozzle tip [36,43,44]. This paper presents a novel statistical/numerical model of the powder-gas jet as a key element of a comprehensive process model for the EHLA process. The underlying assumptions for this model have been derived from experimental observations and are based on images of the PDD captured at various levels with a laser-light sectioning device. It can serve to map the PDD of the powder-gas flow, the powder mass flows, and carrier and inert gas settings to a theoretical model.

2. Materials and Methods

2.1. Powdered Additive

The procedure for modeling PDD was demonstrated using powders sourced from the nickel-based superalloy material no. 2.4856 (similar to: Inconel 625, Special Metals Corporation, New Hartford, USA) with a nominal particle size distribution of −53 + 20 µm (trade name: MetcoClad 625F, made by Oerlikon Metco AG, Wohlen, Swiss) as an example. A scanning electron microscope served to investigate the powder particles' morphology. Figure 4 shows two images of the powder material taken with a scanning electron microscope (SEM) [1].

The powder particles are predominantly spherical. The satellites sporadically appearing on the surface are a result of the powder being produced by gas atomization. The particle size distribution was measured with a statistical image analysis at 20× magnification (Morphologi G3, Malvern Panalytical GmbH, Kassel, Germany). Figure 5 shows the measured relative F_{rel} and cumulative number-weighted frequency distributions F_{abs} against the equivalent diameter d_{CE}. The mean grain diameter is around 35 µm. In keeping with the number-weighted quantiles, around 96.5% of the measured particle diameters are within the manufacturer's specification [1].

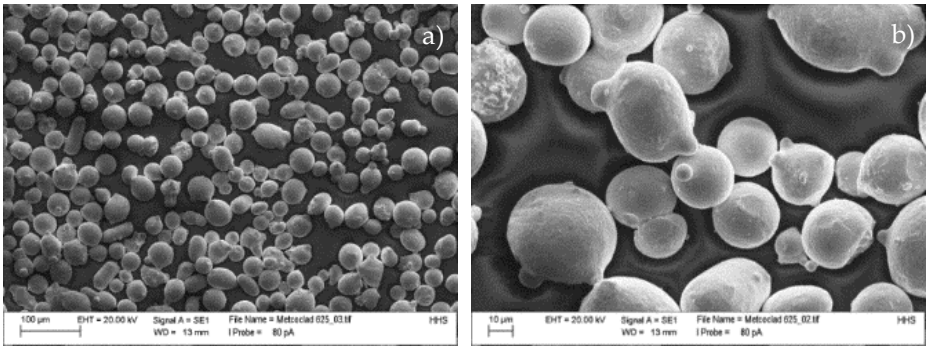

Figure 4. Scanning electron microscope (SEM) images of the powder with −53 + 20 µm grain fraction [1], (**a**) Overview; (**b**) Detail. Reprinted with permission from Ref [1]. Copyright 2020, Fraunhofer Verlag.

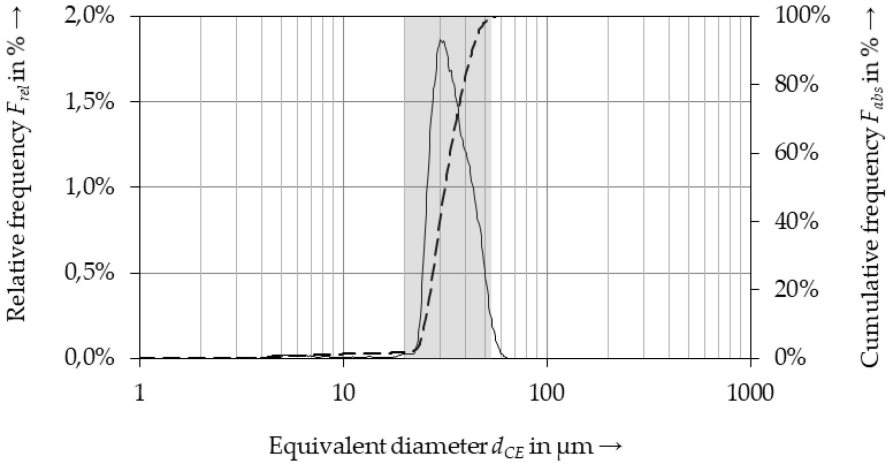

Figure 5. Relative F_{rel} and cumulative number-weighted frequency distributions F_{abs} against the equivalent diameter d_{CE}. Gray box: Manufacturer's specification with grain fraction −53 + 20 µm, mean grain diameter: 35.28 µm [1]. Reprinted with permission from Ref [1]. Copyright 2020, Fraunhofer Verlag.

2.2. Powder Feed

The powder was delivered by a type PF2/2 pneumatic powder feeder made by GTV Verschleißschutz GmbH (Luckenbach, Germany) with feed disc groove size of 0.6 × 5 mm D × W. A type GTV 108 electric mass flow controller made by Bronkhorst Mättig GmbH (Kamen, Germany) integrated into the powder feeder controlled the carrier gas's volume flow. A type GCR-C9SA-BA30 thermal mass flow controller made by Voigtlin Instruments AG (Aesch, Swiss) served to vary the inert gas volume flow. The carrier and shielding gas used for all experiments was argon with a primary pressure of four bar. The powder mass flow rate was measured gravimetrically for each powder grain fraction by weighing the powder quantity conveyed within one minute using a type LSM 200 precision scale (reproducibility 0.01 g) made by PCE GmbH (Meschede, Germany). Figure 6 shows the results of powder mass flow measurements $\dot{m}_p$ taken for one variation of the rotational speed U_P of the powder feed disc from 2 to 8 min^{-1} at a carrier gas volume flow of V_{FG} = 5 L/min.

The data points are the arithmetic mean of three measurements each. The investigation conducted for this paper used a constant carrier gas volume flow of 5 L/min and a shielding gas volume flow of 10 L/min. The required rotational speed of the powder feed disc UP was calculated with the given regression equations [1].

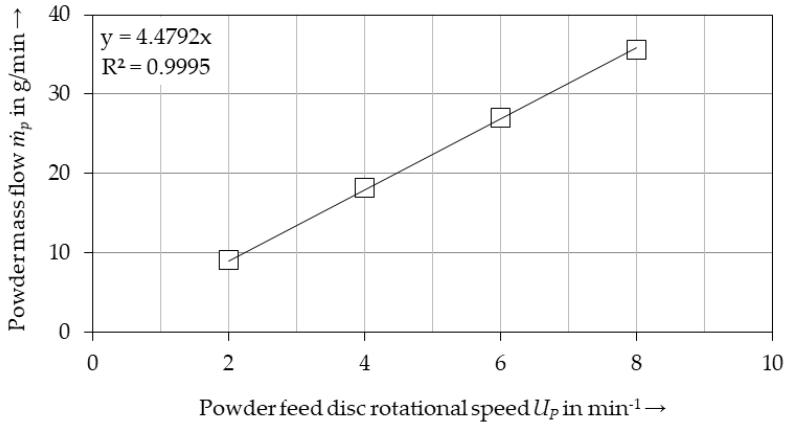

Figure 6. Measured powder mass flow $\dot{m}_p$ in relation to the powder feed disc rotational speed U_p with a grain fraction of −53 +20 µm [1]. Reprinted with permission from Ref [1]. Copyright 2020, Fraunhofer Verlag.

2.3. Powder Nozzle

An ILT-COAX 40-F powder nozzle (Fraunhofer ILT, Aachen, Germany) was used for these investigations. For this nozzle there is a splitter that divides the powder-gas jet into three partial jets that feed into an annular cavity sited between its inner and outer cones. The powder particles collide with the surface of the inner cone and flow with the carrier gas towards the nozzle's tip. This type of powder nozzle forms a hollow powder-gas cone. The powder-gas jet is focused on the tip of this cone (powder focus). Figure 7 diagrams this coaxial nozzle's structure. The width of the annular cavity's gap may be adjusted to the grain fraction and the powder mass flow by twisting the two interlocking cones of the coaxial powder nozzle. The larger the grain fraction and the greater the volume of the powder mass flow, the wider this gap has to be to prevent powder particles clogging the annular cavity between the inner and outer cones. Observations made during preliminary trials with the highest possible rotational speed of the powder feed disc of U_P = 10 min^{-1} revealed that the annular cavity was no longer clogged at a gap width of 179 µm. The gap width of the annular cavity in the direction of flow was therefore around 179 µm for this investigation [1]. See Figure 7 for more on this.

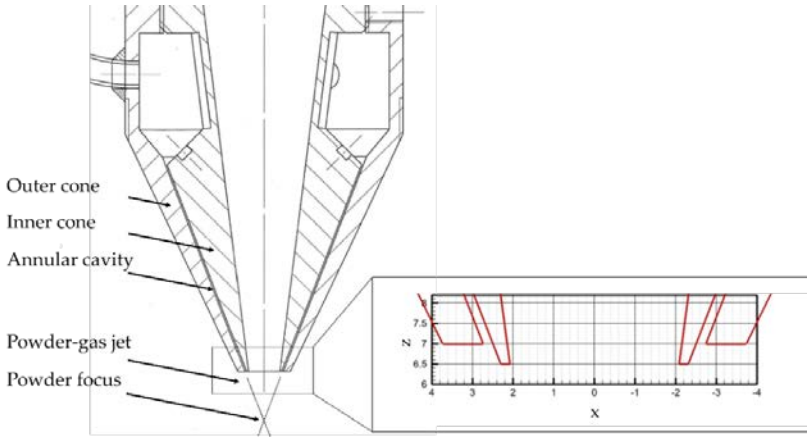

Figure 7. Schematic diagram of the powder nozzle and the annular cavity between the inner and outer cone of the continuous coaxial powder nozzle ILT-COAX 40-F [1]. Reprinted with permission from Ref [1]. Copyright 2020, Fraunhofer Verlag.

2.4. Powder-Gas Jet Ccharacterization

The metrological characterization of PDD was carried out with a laser light-sectioning method using an analytical instrument developed and patented by the Fraunhofer Institute for Laser Technology

ILT [45]. This method can measure the number and position of powder particles in the powder-gas flow level by level for various grain fractions, powder mass flows, and carrier and shielding gas settings. The powder-gas jet was illuminated laterally by a pulsed laser beam source developed at the Fraunhofer ILT (Aachen, Germany). Its wavelength is 810 nm. Optical components shaped the illuminating laser beam so that the height of the illuminating line in the direction of z was approximately 0.26 mm [1]. A type MC 1362 high-sensitivity, high speed CMOS camera made by Mikrotron GmbH (Unterschleißheim, Germany) was mounted coaxially to the powder nozzle. This camera's measuring range is 256 × 256 pixels at a resolution of 50 px/mm; the pixel size is approximately 19.53 µm. The pulsed illumination with a pulse duration of 0.008 ms enabled the powder particle position to be determined precisely while preventing light trails along the particle trajectory caused by motion blur. On the left of Figure 8 is a diagram of this setup; pictured on the right is the device used to measure the powder-gas jet [1].

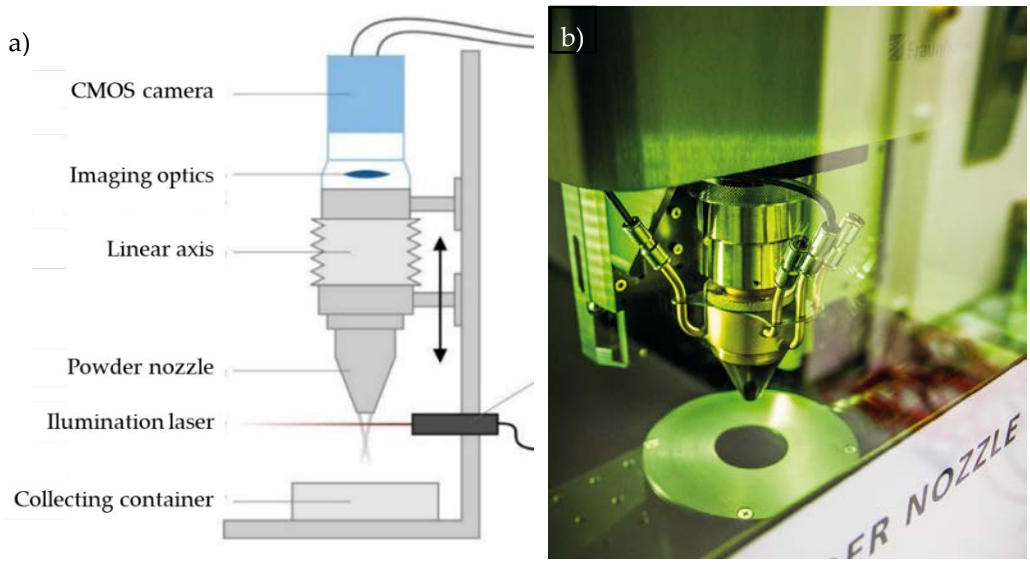

Figure 8. (**a**) Diagram of the experimental setup for measuring the powder-gas jet using the laser light-sectioning method. (**b**) Picture of the measuring device [1]. Reprinted with permission from Ref [1]. Copyright 2020, Fraunhofer Verlag.

Taking shots at a frame rate of 1000 frames per second, the camera can capture the number and position of powder particles at the respective level at a defined time. The powder nozzle was guided in alignment with the linear laser beam and photographed for three seconds at a time. This produced 3000 individual images per level with grayscale values ranging from 0 to 255 for each pixel of the camera chip. Figure 9 shows examples of individual images of the respective levels taken at a distance of 2 mm (E2) to 11 mm (E11) from the nozzle tip at a powder mass flow rate of 5 g/min [1].

The powder's annular distribution is visible when the 3000 individual images taken at each level are superimposed as shown in Figure 10. The powder distribution is no longer annular at a point below the powder focus level somewhere between E7 and E8. If the powder mass flow rate, powder grain fraction and illumination line height in the direction of z are known, then the powder particles' velocities can be approximated with a calculation based on the mean number of particles in the illuminated area [1].

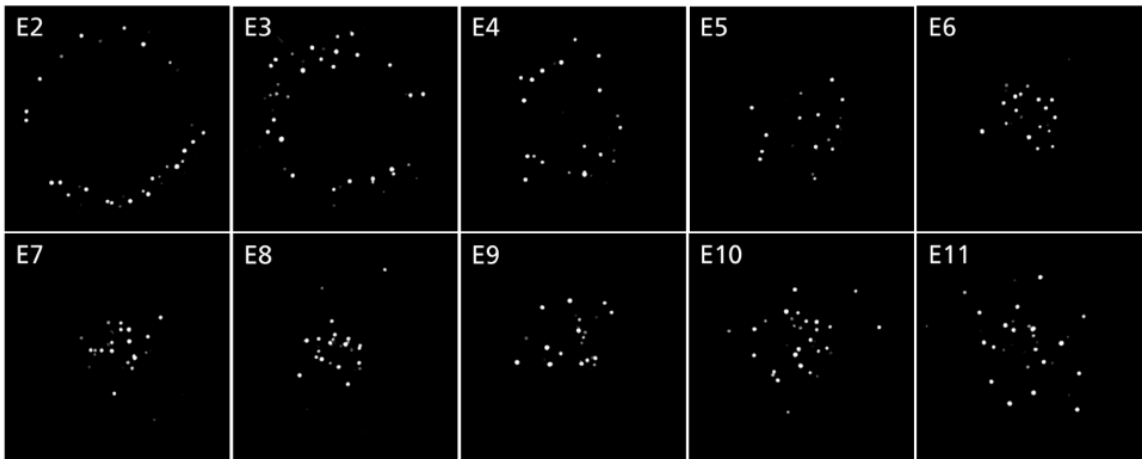

Figure 9. Selected examples of individual pictures of powder-gas jet measurements taken at a distance of 2 mm (**E2**) to 11 mm (**E11**). ILT-COAX 40-F powder nozzle. Parameters: grain fraction −53 + 20 µm, $\dot{m}_p$ = 5 g/min, V_{FG} = 5 L/min, V_{SG} = 10 L/min [1]. Reprinted with permission from Ref [1]. Copyright 2020, Fraunhofer Verlag.

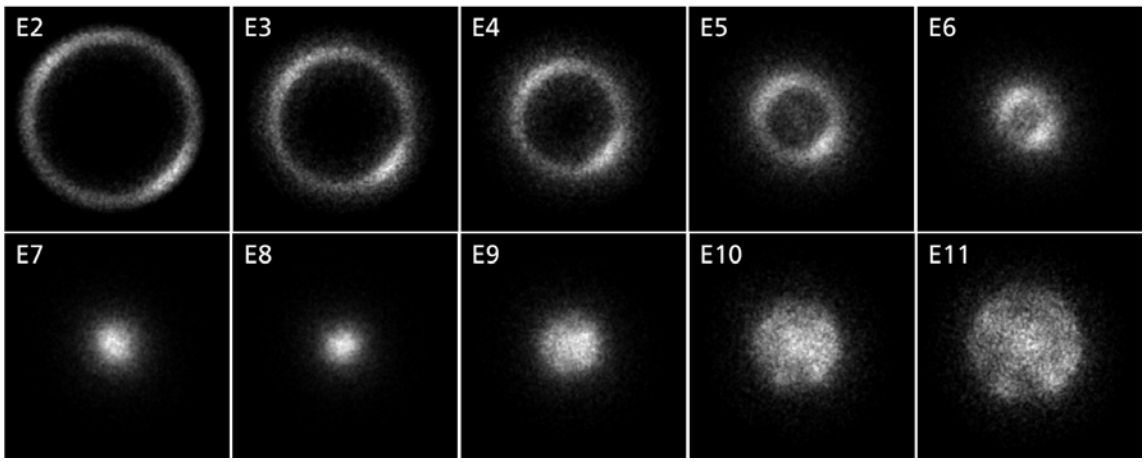

Figure 10. 3000 superimposed images, each of powder-gas jet measurements taken at a distance of 2 mm (E2) to 11 mm (E11). ILT-COAX 40-F powder nozzle. Parameters: grain fraction -53 + 20 µm, $\dot{m}_p$ = 5 g/min, V_{FG} = 5 L/min, V_{SG} = 10 L/min [1]. Reprinted with permission from Ref [1]. Copyright 2020, Fraunhofer Verlag.

3. Result

3.1. Powder Particle Count

A quantitative analysis can determine the number and position of particles in each image as depicted in Figure 9. Contiguous areas were designated as one particle each based on a threshold grayscale value. Figure 11 shows an example of particle identification on the basis of a threshold grayscale value for three individual images each at levels E3 and E4 at a powder mass flow of 5 g/min. The powder nozzle's conical design causes the expansion of the annular particle density at the nozzle outlet to decrease progressively until the powder focus is achieved. The particle density increases continuously as the distance from the powder nozzle tip grows. The greater the particle density, the higher the probability that the projections of two or more particles in the x-y plane overlap within the z measuring plane, and the fewer particles can be identified individually or the more particles are erroneously identified as one particle (particle–particle shading) [1].

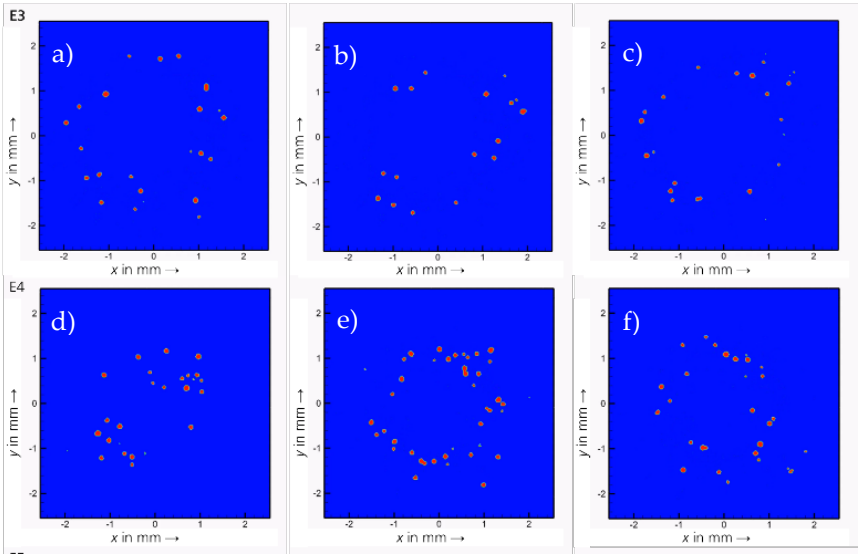

Figure 11. Diagrams of particle identification for each image based on a threshold for the grayscale value of the individual images. Parameters: grain fraction −53 + 20 µm, $\dot{m}_p$ = 5 g/min, V_{FG} = 5 L/min, V_{SG} = 10 L/min, (**a**–**c**): Level E3; (**d**–**f**): Level E4 [1]. Reprinted with permission from Ref [1]. Copyright 2020, Fraunhofer Verlag.

Further factors influencing the particle density–that is, the measured number of particles–within a single image using this measuring method are [1]:

- The height of the illumination line or the measured level (here: 0.26 mm): The greater the height of the illumination line in the direction of z, the greater the number of simultaneously illuminated particles and, as a result, the higher the particle count within the measured level.
- Exposure time: The longer the exposure time (here: 0.008 ms), the greater the motion blur caused by light trails, which means that fewer particles can be identified.
- Resolution of the camera chip: The higher the resolution of the camera chip (here: 19.83 µm/pixel), the more likely it is that non-contiguous areas can be identified as individual particles.
- Distance of the measured level from the powder focus level: The shorter the distance between the measured level and the powder focus level, the greater the particle densities. The reason for this is that the particle count within the measured level decreases as the area of the powder-gas jet cross-section decreases.
- Grain fraction: The smaller the grain fraction, the higher the particle count at the same powder mass flow rate due to the proportionality to $1/r_p{}^3$, and the fewer the particles that can be identified individually.
- Particle velocity: The lower the particle velocity, the greater the number of simultaneously illuminated particles and the higher the particle count.
- Powder mass flow: The greater the powder mass flow, the higher the particle count in the measuring level at the same powder grain fraction.

Figure 12 shows an example of the overlap of several particles in the x-y plane within a single image. Starting at level E6, the number of particles detected for the investigated powder mass flows was significantly lower than at level E3. This is attributable to the increasing particle density along the beam axis caused by the decreasing area of the powder-gas jet cross-section and the resultant increasing overlap of particles [1].

For this reason, E3 serves in the following as a reference level to determine the mean particle count per level. The powder particle density distribution in the levels below the z plane is described with the help of a statistical model for the particle trajectories. See Section 3.3 for more on this. For example,

the mean measured particle count per individual image is 68 for a powder mass flow rate of 15 g/min, a carrier gas volume flow rate of 5 L/min and an inert gas volume flow rate of 10 L/min [1].

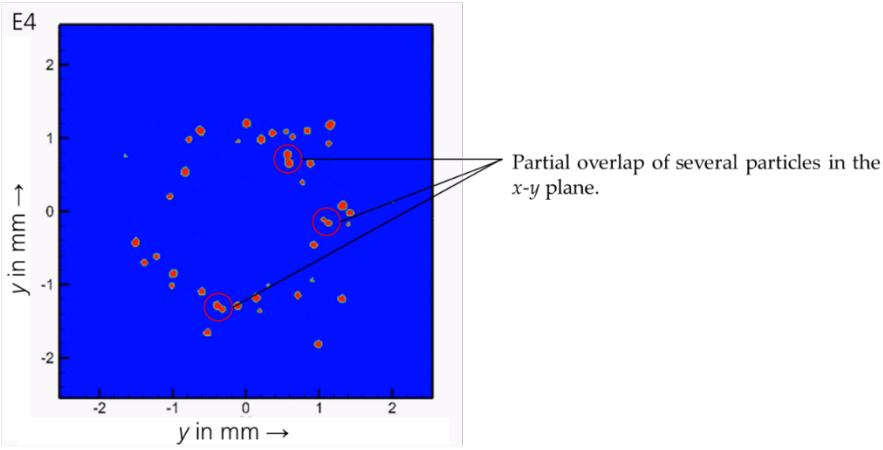

Figure 12. Diagram of the partial overlap in the x-y plane within a single image in level E4. Parameters: grain fraction −53 + 20 µm, $\dot{m}_p$ = 5 g/min, V_{FG} = 5 L/min, V_{SG} = 10 L/min [1]. Reprinted with permission from Ref [1]. Copyright 2020, Fraunhofer Verlag.

3.2. Approximation of the Particle Velocity

The number of particles n in a given volume can generally be expressed by the volume integral of the particle density distribution of the powder-gas jet $n(x,y,z)$, as expressed by Equation (2) [1]:

$$n = \int n(x,y,z)dxdydz. \tag{2}$$

Equation (4) expresses the number of particles n at the height of measuring level Δz [1]:

$$\frac{n}{\Delta z} = \int n(x,y,z)dxdy. \tag{3}$$

The powder mass flow $\dot{m}_p$ is equal to the mean particle number per level multiplied by the powder mass of a single particle m_p with the mean particle velocity $\overline{v}_p$ as expressed in Equation (5) [1]:

$$\dot{m}_p = \frac{n}{\Delta z} m_p \overline{v}_p. \tag{4}$$

This results in the mean particle velocity $\overline{v}_p$ as expressed by Equation (6) [1]:

$$\overline{v}_p = \frac{\Delta z\, \dot{m}_p}{n\, m_p} \tag{5}$$

Based on the aforementioned mean measured particle number per single image for a powder mass flow of 15 g/min, a carrier gas volume flow of 5 L/min and an inert gas volume flow of 10 L/min, the average particle velocity is $\overline{v}_p = 4.908$ m/s [1].

3.3. Particle Propagation Model

Particle–particle shading yields excessive particle densities (see Section 3.1) that skew the particle count so their numbers cannot be measured with sufficient accuracy at every level. Pictures of the powder-gas jet taken with a high-speed camera show that the trajectories of the particles after they exit the nozzle aperture are rectilinear until they make contact with the substrate. This allows for an explicit representation of the particle trajectories and velocities in a statistical model. High-speed

images of the powder-gas jet also confirm the assumptions that the particle velocity is constant and the propagation is linear. Figure 13 shows an example of a high-speed, multiple-exposure image of the powder-gas jet at a powder mass flow rate of 5 g/min, which is in line with the investigated process parameter range. The picture was taken with a Photron FASTCAM SA5 camera made by VKT Video Kommunikation GmbH (Pfullingen, Germany). The points are on a line (rectilinear propagation) and separated by an approximately constant distance (constant particle velocity) [1].

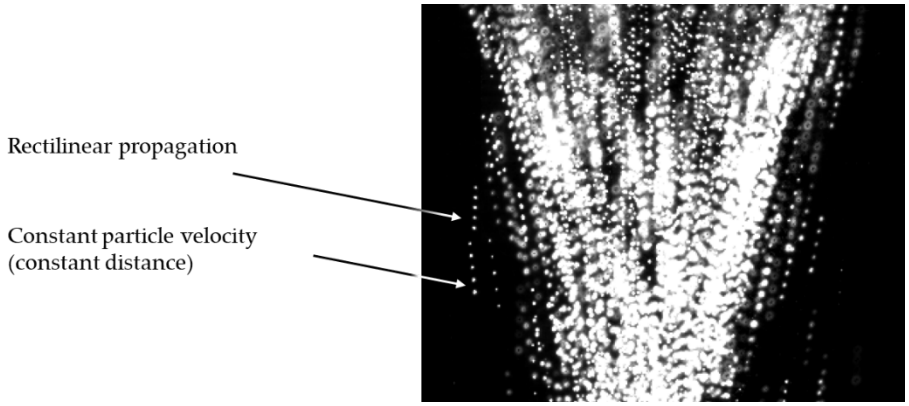

Figure 13. Images of the powder-gas jet taken at high speed with multiple exposures. Parameters: grain fraction −53 + 20 µm, $\dot{m}_p$ = 5 g/min, V_{FG} = 5 L/min, V_{SG} = 10 L/min [1]. Reprinted with permission from Ref [1]. Copyright 2020, Fraunhofer Verlag.

A statistical description of the particles' trajectories requires figures for the distribution of starting points and direction of flight at the nozzle aperture. A particle's direction is determined by a directional vector given by the nozzle's angle of inclination. It is inclined in two perpendicular directions (see the diagram on the left of Figure 14). An initial distribution with an ensemble of $5{\cdot}10^5$ particles is predetermined at the nozzle outlet surface. Constrained by the nozzle walls ($r_1 < r < r_2$), this distribution has a Gaussian shape with respect to r and is uniform with respect to Φ. The inclination angles in this initial distribution are predetermined with respect to β $N(\beta, \Delta\beta^2)$ and γ normally distributed $N(0, \Delta\gamma^2)$. The starting points at the nozzle aperture are evenly distributed around the annular gap. The number of particles per second derives from the powder mass flow and the mean particle diameter. The resultant particle density in the reference level is calculated based on this input data. This does not correspond to the measured distribution, but should be covered by a suitable choice of γ and β. See the diagram on the left of Figure 15 [1].

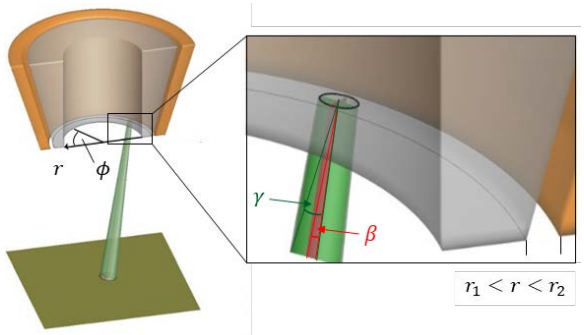

Figure 14. Diagram of the parameters for the particle propagation model. Left: Description of the powder particle density distribution with polar coordinates (r,Φ). Right: Model parameters for adjusting the angles inclination with respect to the z-axis: β and the x-y-axis: γ [1]. Reprinted with permission from Ref [1]. Copyright 2020, Fraunhofer Verlag.

In the next step, the calculated frequency distribution is normalized to one—that is, the maximum value is equal to one. A sequence of equally distributed random numbers in the range of [0,1] with the same length as the statistical particle ensemble is then generated. Each particle is assigned the corresponding random number from this sequence. If the random number for the particle lies above the normalized measured distribution, the particle is removed from the list. The remaining particles constitute a particle density at level E3 approximating the measured particle density. Figure 15 shows an example of the result of an adjustment made to model parameters β and γ and the filtering of trajectories for the particle density distribution of a powder-gas jet with a powder mass flow rate of 5 g/min at level E3 [1].

Non-uniform rational basis splines (NURBS) are also applied to smooth the measured particle density distribution. The graph on the left in Figure 16 shows an example of the modeled powder-gas jet with a powder mass flow of 5 g/min at a distance of up to 8 mm from the nozzle's tip. The center diagram shows the modeled particle density distributions. On the right is the composite of 3000 individual pictures of powder-gas jet measurements taken at levels E3 and E8 with the laser-light sectioning method. The result is a numerical description of the particle trajectories that takes into account the measured particle size distribution with calculations made on the assumption of a constant particle velocity and linear trajectories of the particles [1].

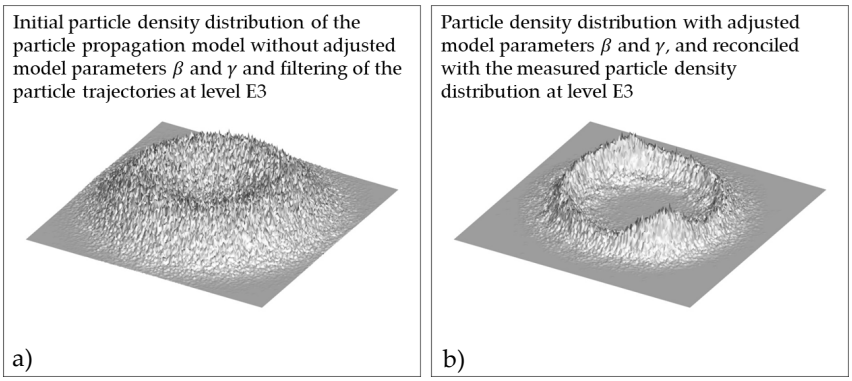

Figure 15. (**a**) Particle density distribution with a suitable selection of model parameters β and γ at level E3 and on the basis of the initial distribution, which is Gaussian with respect to r and uniform with respect to φ. (**b**) Particle density distribution after a statistical filtering of particle trajectories [1]. Reprinted with permission from Ref [1]. Copyright 2020, Fraunhofer Verlag.

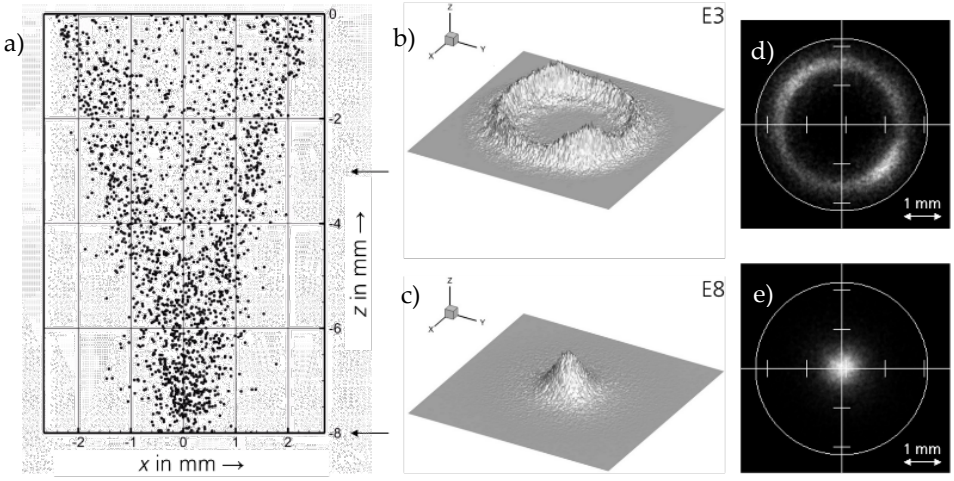

Figure 16. (**a**) Lateral view of the simulated powder-gas jet; (**b**,**c**): Simulated particle density distribution for levels E3 and E8. (**d**,**e**) 3000 superimposed images of measurements for levels E3 and E8. Parameters: grain fraction −53 + 20 µm, $\dot{m}_p$ = 5 g/min, V_{FG} = 5 L/min, V_{SG} = 10 L/min [1]. Reprinted with permission from Ref [1]. Copyright 2020, Fraunhofer Verlag.

3.4. Powder Particle Density Distribution

The statistical model for particle trajectories can also serve to determine the particle density for areas in which the particle density cannot be measured directly because of the partial particle overlap in the *x*-*y*-plane resulting from the decreasing area of the powder-gas jet cross section. A probability density was determined for each level to enable comparisons of the powder-gas jet's particle density distribution along the beam's propagation trajectory at various powder feed settings. The integral of the density distribution was normalized to a value of 1 via dx, dy to this end. The powder particle density distribution in absolute units of particles per cubic millimeter can be calculated by multiplying the probability density by the height of the illuminating laser beam dz, and normalizing it to the number of particles per level. Figure 17 shows an example of the modeled probability density for the reference setting as a function of the working distance between $z = -3$ mm and $z = -14$ mm by levels (left) and by x = const. (right). The powder particle density progresses from an annular distribution at the nozzle aperture to a centered distribution at the focus of the powder jet in the direction of the beam. The powder-gas jet widens continuously along the levels below the powder focus relative to the beam axis [1].

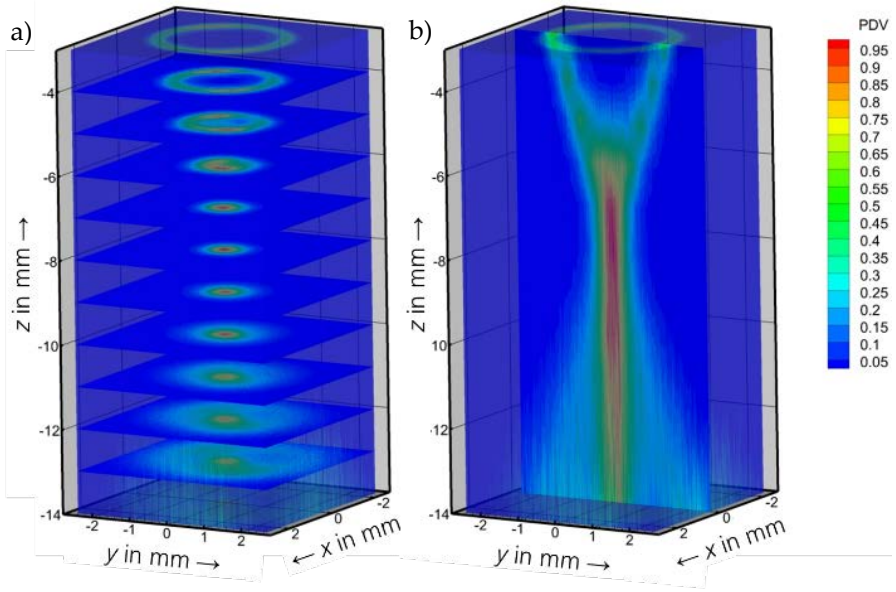

Figure 17. (**a**) level-wise probability density as a function of the working distance 7 = const., (**b**) level by level probability density as a function of the working distance for × = const. Parameters: grain fraction -53 + 20 µm, $\dot{m}_p$ = 15 g/min, V_{FG} = 5 L/min [1]. Reprinted with permission from Ref [1]. Copyright 2020, Fraunhofer Verlag.

Pictured on the left of Figure 18 are lateral views of examples of the modeled powder-gas jet for different grain size distributions. On the right side are coaxial views of the powder-gas jet up to a distance of 8 mm from the nozzle tip (E8) with a laser beam diameter of d_L = 1.13 mm at the processing level (red). A drastic increase in particle density is clearly visible despite the comparable probability densities. This is the result of the particle count increasing as the mean particle diameter decreases [1].

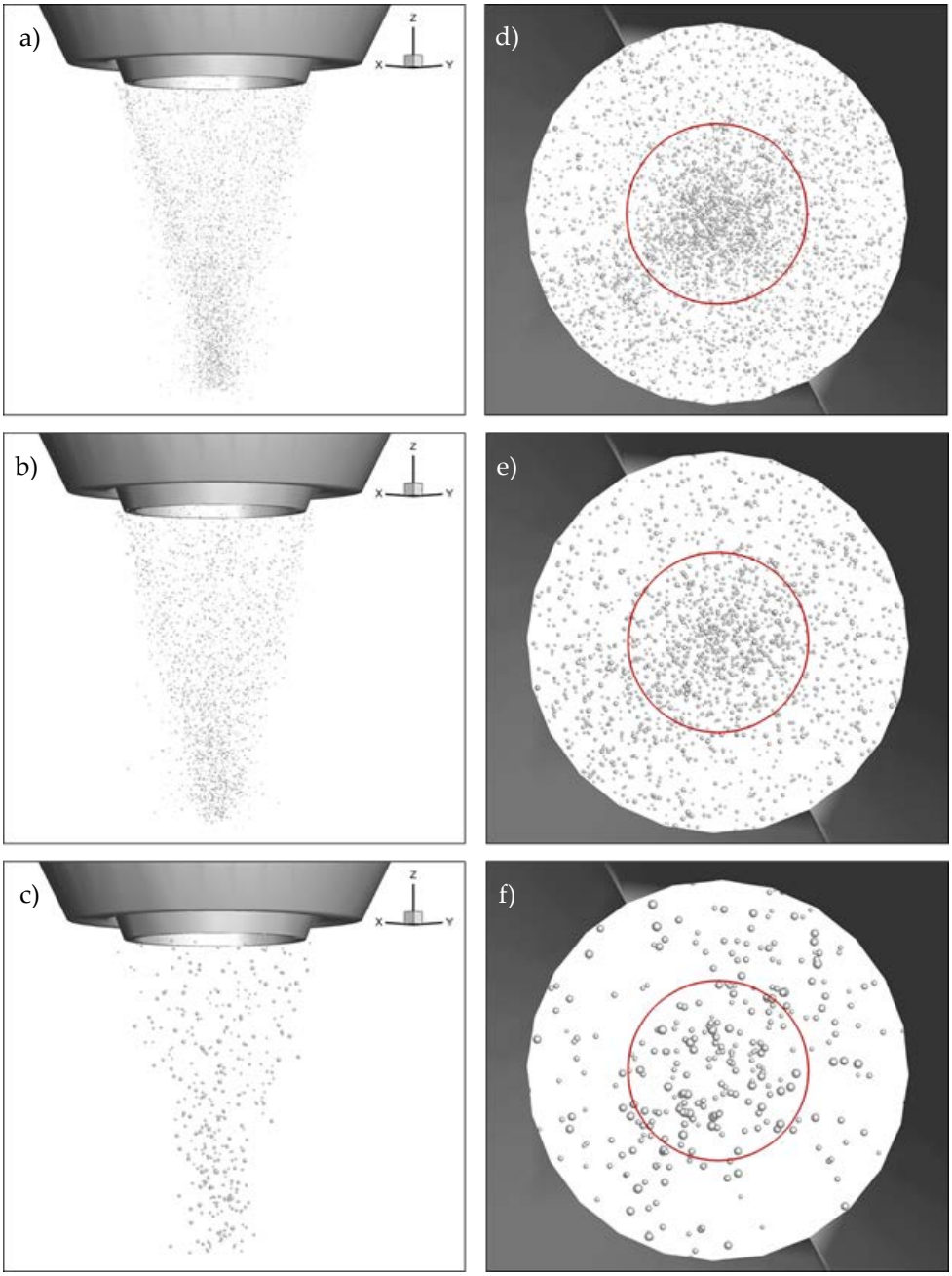

Figure 18. (**a**–**c**): Lateral views of the simulated powder-gas jet up to level E8. (**d**–**f**): Coaxial views of the powder-gas beam for level E8, red: laser beam. Grain fractions at the top: −45 + 11 µm, center: −53 + 20 µm, bottom: −90 + 45 µm. Parameters: $\dot{m}_p$ = 15 g/min, V_{FG} = 5 L/min, V_{SG} =10 L/min [1]. Reprinted with permission from Ref [1]. Copyright 2020, Fraunhofer Verlag.

4. Conclusions and Outlook

- The number and position of powder particles in the powder-gas flow can be determined quantitatively, level by level, with a measuring device based on the laser-light sectioning method.
- Pictures of the powder-gas jet taken with a high-speed camera serve to show that the trajectories of the particles after they exit the nozzle outlet are rectilinear and travel at a constant velocity until they contact the substrate. This allows for an explicit representation of the particle trajectories and velocities in a statistical model.

- The model theory-based description of the PDD presented in this paper is a key component of a comprehensive EHLA process model, as published in [1]. This serves to map the PDD of the powder-gas flow—and particularly the particle trajectories for different grain fractions—as well as the powder mass flows and carrier and inert gas settings to a theoretical model.
- In a further step the laser radiation will be characterized experimentally and mapped to the mathematical model.
- Based on this breakdown the interaction between the laser beam and the powder particles can be described. This enhances the understanding of the process-relevant influencing factors such as laser beam transmittance via the powder-gas jet, particle heating in the beam path, substrate heating and track formation.
- The transmitted laser intensity distribution and mean particle temperature are used as boundary conditions for the governing equations of the mathematical model for the track formation.
- This model will provide the means to assess the EHLA process's technological limits, for example, in terms of the achievable feed rate and track formation, and to push beyond these boundaries to effectively extend this process's range of potential manufacturing applications, particularly in surface engineering, but also in repair and additive manufacturing.

Author Contributions: Conceptualization, T.S.; methodology, T.S., N.P. and S.M.; software, N.P. and S.M.; T.S.; writing—original draft preparation, T.S.; writing—review and editing, N.P., S.M., R.P., C.L.H. and J.H.S.; visualization, N.P., and S.M.; supervision, R.P., C.L.H., and J.H.S.; project administration, T.S.; All authors have read and agreed to the published version of the manuscript.

Funding: This research received no external funding.

Acknowledgments: In adherence to the rules of good scientific practice it is stated, that the presented numerical model of the powder-gas jet for Extreme High-Speed Laser Material Deposition has been previously published in [1] in German language as part of a Ph.D. thesis. This publication serves to make the developed model available to a larger, international audience.

Conflicts of Interest: The authors declare no conflict of interest.

References

1. Schopphoven, T. Experimentelle und Modelltheoretische Untersuchungen zum Extremen Hochgeschwindigkeits-Laserauftragschweißen. Ph.D. Thesis, RWTH Aachen University, Aachen, Germany, 2020.
2. Pirch, N.; Linnenbrink, S.; Gasser, A.; Wissenbach, K.; Poprawe, R. Analysis of track formation during laser metal deposition. *J. Laser Appl.* **2017**, *29*, 022506. [CrossRef]
3. Pirch, N.; Niessen, M.; Linnenbrink, S.; Schopphoven, T.; Gasser, A.; Poprawe, R.; Schulz, W. Temperature field and residual stress distribution for laser metal deposition. *J. Laser Appl.* **2018**, *30*, 032503. [CrossRef]
4. Poprawe, R.; Hinke, C.; Meiners, W.; Eibl, F.; Zarei, O.; Voshage, M.; Willenborg, E.; Ziegler, S.; Schleifenbaum, J.H.; Gasser, A.; et al. Digital photonic production along the lines of industry 4.0. In *Laser Applications in Microelectronic and Optoelectronic Manufacturing (LAMOM) XXIII*; International Society for Optics and Photonics: San Francisco, CA, USA, February 2018; Volume 10519, p. 1051907.
5. Schopphoven, T.; Gasser, A.; Backes, G. EHLA: Extreme High-Speed Laser Material Deposition: Economical and effective protection against corrosion and wear. *Laser Technik J.* **2017**, *14*, 26–29. [CrossRef]
6. Schopphoven, T.; Gasser, A.; Wissenbach, K.; Poprawe, R. Investigations on ultra-high-speed laser material deposition as alternative for hard chrome plating and thermal spraying. *J. Laser Appl.* **2016**, *28*, 022501. [CrossRef]
7. Fraunhofer Gesellschaft zur Forderung der Angewandten Forschung. Extremes Hochgeschwindigkeitslaserauftragschweißverfahren. DE Patent DE 10 2011 100 456 B4, 4 May 2011.
8. Lin, J. Temperature analysis of the powder streams in coaxial laser cladding. *Opt. Laser Technol.* **1999**, *31*, 565–570. [CrossRef]
9. Liu, C.Y.; Lin, J. Thermal processes of a powder particle in coaxial laser cladding. *Opt. Laser Technol.* **2003**, *35*, 81–86. [CrossRef]

10. Ibarra-Medina, J.; Pinkerton, A.J. A CFD model of the laser, coaxial powder stream and substrate interaction in laser cladding. *Phys. Procedia* **2010**, *5*, 337–346. [CrossRef]
11. Ibarra-Medina, J.; Pinkerton, A.J. Numerical investigation of powder heating in coaxial laser metal deposition. *Surf. Eng.* **2011**, *27*, 754–761. [CrossRef]
12. Zhang, K.; Zhang, X.M.; Liu, W.J. Influences of Processing Parameters on Dilution Ratio of Laser Cladding Layer during Laser Metal Deposition Shaping. *Adv. Mater. Res.* **2012**, *549*, 785–789. [CrossRef]
13. Gasser, A.; Meiners, W.; Weisheit, A.; Willenborg, E.; Stollenwerk, J.; Wissenbach, K. Tailor-made surfaces and components—The use of laser radiation in surface technology and rapid manufacturing—Part 1. *Laser-Tech. J.* **2010**, *7*, 47–53. [CrossRef]
14. Beyer, E.; Wissenbach, K. *Oberflächenbehandlung mit Laserstrahlung*; Springer-Verlag: Berlin, Germany, 1998; Volume 7, pp. 243–251. [CrossRef]
15. Partes, K.; Seefeld, T.; Sepold, G.; Vollertsen, F. Increased efficiency in laser cladding by optimization of beam intensity and travel speed. In *Workshop on Laser Applications in Europe*; International Society for Optics and Photonics: Dresden, Germany, December 2005; Volume 6157, p. 615700.
16. Partes, K. High-Speed Coating with the Laser Beam. Ph.D. Thesis, Bremer Institut für Angewandte Strahltechnik, Bremen, Germany, 2008.
17. Peyre, P.; Aubry, P.; Fabbro, R.; Neveu, R.; Longuet, A. Analytical and numerical modelling of the direct metal deposition laser process. *J. Phys. D Appl. Phys.* **2008**, *41*, 025403. [CrossRef]
18. Liu, H.; He, X.; Yu, G.; Wang, Z.; Li, S.; Zheng, C.; Ning, W. Numerical simulation of powder transport behavior in laser cladding with coaxial powder feeding. *Sci. China Phys. Mech. Astron.* **2015**, *58*, 104701. [CrossRef]
19. Kussin, J. Experimental Studies on Particle Movement and Turbulence Modification in a Horizontal Channel with Different Wall Roughness. Ph.D. Thesis, Martin-Luther-Universität Halle-Wittenberg, Halle, Germany, 2004.
20. Kovalev, O.B.; Zaitsev, A.V.; Novichenko, D.; Smurov, I. Theoretical and experimental investigation of gas flows, powder transport and heating in coaxial laser direct metal deposition (DMD) process. *J. Therm. Spray Technol.* **2011**, *20*, 465–478. [CrossRef]
21. Pan, H.; Liou, F. Numerical simulation of metallic powder flow in a coaxial nozzle for the laser aided deposition process. *J. Mater. Process. Technol.* **2005**, *168*, 230–244. [CrossRef]
22. Pan, H.; Sparks, T.; Thakar, Y.D.; Liou, F. The investigation of gravity-driven metal powder flow in coaxial nozzle for laser-aided direct metal deposition process. *J. Manuf. Sci. Eng.* **2006**, *128*, 541–553. [CrossRef]
23. Elghobashi, S. On predicting particle-laden turbulent flows. *Appl. Sci. Res.* **1994**, *52*, 309–329. [CrossRef]
24. Wibel, W. Studies on Laminar, Transitional and Turbulent Flow in Rectangular Microchannels. Ph.D. Thesis, Technische Universität Dortmund, Dortmund, Germany, 2009.
25. Kravtsov, M.V. Resistance to the free steady-state motion of a sphere in a viscous medium. *J. Eng. Phys. Thermophys.* **1968**, *15*, 833–838.
26. Li, H.P.; Chen, X. Three-dimensional modeling of the turbulent plasma jet impinging upon a flat plate and with transverse particle and carrier-gas injection. *Plasma Chem. Plasma Process.* **2002**, *22*, 27–58. [CrossRef]
27. Haider, A.; Levenspiel, O. Drag coefficient and terminal velocity of spherical and nonspherical particles. *Powder Technol.* **1989**, *58*, 63–70. [CrossRef]
28. Gerold, J. Experimental and Numerical Investigation of Gas Free Jets. Ph.D. Thesis, Universität der Bundeswehr München, Neubiberg, Germany, 2015.
29. Richter, F.; Leder, A.; Dopheide, D.; Müller, H.; Strunck, V. (Eds.) Wechselwirkungen runder Düsenfreistrahlen mit ebenen Wänden. In Proceedings of the Fachtagung "Lasermethoden in der Strömungstechnik", Braunschweig, Germany, 7–9 September 2006.
30. Rajaratnam, N. *Turbulent Jets*; Elsevier: Amsterdam, The Netherlands, 1976; Volume 5.
31. Wen, S.Y.; Shin, Y.C.; Murthy, J.Y.; Sojka, P.E. Modeling of coaxial powder flow for the laser direct deposition process. *Int. J. Heat Mass Transf.* **2009**, *52*, 5867–5877. [CrossRef]
32. Lin, J. Numerical simulation of the focused powder streams in coaxial laser cladding. *J. Mater. Process. Technol.* **2000**, *105*, 17–23. [CrossRef]
33. Tabernero, I.; Lamikiz, A.; Ukar, E.; de Lacalle, L.L.; Angulo, C.; Urbikain, G. Numerical simulation and experimental validation of powder flux distribution in coaxial laser cladding. *J. Mater. Process. Technol.* **2010**, *210*, 2125–2134. [CrossRef]

34. Zhang, A.; Li, D.; Zhou, Z.; Zhu, G.; Lu, B. Numerical simulation of powder flow field on coaxial powder nozzle in laser metal direct manufacturing. *Int. J. Adv. Manuf. Technol.* **2010**, *49*, 853–859. [CrossRef]
35. Kovalev, O.B.; Kovaleva, I.O.; Smurov, I.Y. Numerical investigation of gas-disperse jet flows created by coaxial nozzles during the laser direct material deposition. *J. Mater. Process. Technol.* **2017**, *249*, 118–127. [CrossRef]
36. Yang, N. Concentration model based on movement model of powder flow in coaxial laser cladding. *Opt. Laser Technol.* **2009**, *41*, 94–98. [CrossRef]
37. Qi, H.; Mazumder, J.; Ki, H. Numerical simulation of heat transfer and fluid flow in coaxial laser cladding process for direct metal deposition. *J. Appl. Phys.* **2006**, *100*, 024903. [CrossRef]
38. Liu, S.; Zhang, Y.; Kovacevic, R. Numerical simulation and experimental study of powder flow distribution in high power direct diode laser cladding process. *Lasers Manuf. Mater. Process.* **2015**, *2*, 199–218. [CrossRef]
39. Diniz Neto, O.O.; Alcalde, A.M.; Vilar, R. Interaction of a focused laser beam and a coaxial powder jet in laser surface processing. *J. Laser Appl.* **2007**, *19*, 84–88. [CrossRef]
40. Pinkerton, A.J. An analytical model of beam attenuation and powder heating during coaxial laser direct metal deposition. *J. Phys. D Appl. Phys.* **2007**, *40*, 7323. [CrossRef]
41. Pinkerton, A.J.; Li, L. Modelling powder concentration distribution from a coaxial deposition nozzle for laser-based rapid tooling. *J. Manuf. Sci. Eng.* **2004**, *126*, 33–41. [CrossRef]
42. Pinkerton, A.J.; Li, L. A verified model of the behaviour of the axial powder stream concentration from a coaxial laser cladding nozzle. In *Proceedings of ICALEO*; Laser Institute of America: Orlando, FL, USA, 2002; Volume 2.
43. Lin, J.; Hwang, B.C. Coaxial laser cladding on an inclined substrate. *Opt. Laser Technol.* **1999**, *31*, 571–578. [CrossRef]
44. Liu, J.; Li, L.; Zhang, Y.; Xie, X. Attenuation of laser power of a focused Gaussian beam during interaction between a laser and powder in coaxial laser cladding. *J. Phys. D Appl. Phys.* **2005**, *38*, 1546. [CrossRef]
45. Fraunhofer Gesellschaft zur Forderung der Angewandten Forschung. Method and Device for Detecting a Particle Density Distribution in the Jet of a Nozzle. DE Patent DE102011009345B3, 25 January 2011.

© 2020 by the authors. Licensee MDPI, Basel, Switzerland. This article is an open access article distributed under the terms and conditions of the Creative Commons Attribution (CC BY) license (http://creativecommons.org/licenses/by/4.0/).